



Riker, J. M., Humphreys, M. C. S., Brooker, R., de Hoog, C-J. (2018). First measurements of OH-C exchange and temperature-dependent partitioning of OH and halogens in the system apatite-silicate melt. *American Mineralogist*, 103(2), 260-270. <https://doi.org/10.2138/am-2018-6187CCBY>

Publisher's PDF, also known as Version of record

License (if available):  
CC BY

Link to published version (if available):  
[10.2138/am-2018-6187CCBY](https://doi.org/10.2138/am-2018-6187CCBY)

[Link to publication record in Explore Bristol Research](#)  
PDF-document

## University of Bristol - Explore Bristol Research

### General rights

This document is made available in accordance with publisher policies. Please cite only the published version using the reference above. Full terms of use are available:  
<http://www.bristol.ac.uk/red/research-policy/pure/user-guides/ebr-terms/>

## First measurements of OH-C exchange and temperature-dependent partitioning of OH and halogens in the system apatite–silicate melt<sup>‡</sup>

JENNY RIKER<sup>1,2</sup>, MADELEINE C.S. HUMPHREYS<sup>1,\*</sup>, RICHARD A. BROOKER<sup>2</sup>, JAN C.M. DE HOOG<sup>3</sup>, AND EIMF<sup>3</sup>

<sup>1</sup>Department of Earth Sciences, Durham University, Science Labs, Durham DH1 3LE, U.K.

<sup>2</sup>Department of Earth Sciences, University of Bristol, Queen's Road, Bristol BS8 1RJ, U.K.

<sup>3</sup>Edinburgh Ion Microprobe Facility, School of GeoSciences, University of Edinburgh, The King's Buildings, James Hutton Road, Edinburgh EH9 3FE, U.K.

### ABSTRACT

We present the first integrated study of carbonate, hydroxyl, fluoride, and chloride ion partitioning in the apatite–melt system. We determined volatile partitioning behavior between apatite and silicate melt for both haplobasaltic andesite and trachyte bulk compositions at 0.5–1 GPa and 1250 °C using the piston–cylinder apparatus. All volatile species were analyzed directly in both apatite and glass using secondary ion mass spectrometry (SIMS) and electron probe microanalysis. Distribution coefficients for OH–halogen exchange are similar to those from previous studies, and together with literature data, reveal a significant log–linear relationship with temperature, while the effects of pressure and melt composition are minimal. Meanwhile, halogen-free experiments generate very high C contents (up to 5000 ppm) in apatite. Stoichiometry calculations and infrared spectra indicate that this C is mainly incorporated onto the channel volatile site together with hydroxyl. In halogen-bearing experiments, apatite crystals contain significantly lower C ( $\leq 500$  ppm), which may be partly incorporated onto the phosphate site while the channel volatile site is filled by OH+F+Cl+C. Our experiments give the first constraints on H<sub>2</sub>O–CO<sub>2</sub> exchange between apatite and silicate melt, with a  $K_D$  of  $0.355 \pm 0.05$  for the trachyte and  $0.629 \pm 0.08$  for the haplobasaltic andesite. The new constraints on the temperature-dependence of partitioning will enable quantitative modeling of apatite–volatile exchange in igneous systems, while this new partitioning data and method for direct, in situ analysis of C in apatite mark a significant advance that will permit future studies of magmatic C and other volatiles. This has a broad range of potential applications including magmatic differentiation, fractionation, and degassing; quantification of volatile budgets in extraterrestrial and deep earth environments; and mineralization processes.

**Keywords:** Apatite, volatiles, partitioning, carbon, halogens, water

### INTRODUCTION

Volatile-bearing minerals such as apatite represent a useful source of information about the volatile compositions of the systems from which they crystallize. Apatite has a very flexible mineral structure, and igneous apatites can accommodate all the major volatile species of magmatic importance, i.e., H, C, F, Cl, and S, as well as other trace volatile species such as Br and I (e.g., Peng et al. 1997; Pan and Fleet 2002; Marks et al. 2012; Konecke et al. 2017). With some knowledge of the partitioning properties of these volatiles, apatite may be able to, therefore, provide quantitative information about multi-component degassing, and other processes, in terrestrial magmas. The apatite crystal formula is Ca<sub>5</sub>(PO<sub>4</sub>)<sub>3</sub>X, where X represents the channel volatile site that runs parallel to the crystallographic c-axis and is typically occupied by OH, F, and Cl. While there are several existing studies focusing on exchange between OH and halogens in the channel site (e.g., Mathez and Webster 2005; Webster et al. 2009, 2017; Doherty et

al. 2014; Li and Hermann 2015, 2017; McCubbin et al. 2015; Potts et al. 2015), we are not aware of any previous work quantitatively examining the partitioning behavior of C between apatite and a silicate melt. Knowledge of the C partitioning behavior would be particularly valuable for studies of terrestrial volcanism because magmatic CO<sub>2</sub> contents are difficult to infer using traditional methods such as melt inclusions. The solubility of CO<sub>2</sub> in silicate melts is strongly dependent on pressure, which means that CO<sub>2</sub> is typically degassed very early during magma ascent, and the highest (primary) CO<sub>2</sub> contents are generally thought not to be trapped in melt inclusions, or are lost to shrinkage bubbles (e.g., Bureau et al. 1999; Wallace 2005; Blundy et al. 2010; Hartley et al. 2014; Moore et al. 2015; Wallace et al. 2015; Aster et al. 2016). Furthermore, it is commonly not clear as to the extent to which melt inclusions have been affected either by post-entrapment diffusive modification (e.g., Gaetani et al. 2012) or by fluxing of CO<sub>2</sub>-rich fluids through the magma reservoir during entrapment (e.g., Spilliaert et al. 2006; Collins et al. 2009; Blundy et al. 2010). The existing work on quantitative determination of carbonate contents of apatite is based on FTIR using doubly polished, oriented wafers. This level of sample preparation is almost prohibitively difficult for

\* E-mail: madeleine.humphreys@durham.ac.uk

<sup>‡</sup> Open access: Article available to all readers online. This article is CC-BY.

magmatic apatites, which are typically small microphenocrysts or inclusions in other magmatic mineral phases. Here we successfully determine C in apatite using secondary ion mass spectrometry, and present data from a series of high-pressure and high-temperature experiments allowing us to constrain the combined partitioning behavior of H, C, F, and Cl between apatite and silicate melts.

## EXPERIMENTAL METHODS

Our experimental approach was to examine volatile partitioning and exchange equilibria between apatite and silicate melts, with a particular focus on C and OH. We added halogens (F and Cl) in a subset of runs, to evaluate the extent to which this affects the partitioning of C and/or OH. The terminal run pressures (1.0 and 0.5 GPa) and temperatures (1250 °C) employed represent reasonable storage conditions for mid- to lower-crustal mafic magmas. Our chosen run conditions have the added advantages that (1) apatite + melt are commonly the only phases present, and (2) the glass fraction of run products is typically greater than 50% (e.g., Prowatke and Klemme 2006). These conditions simplify interpretation of the partitioning data and ensure that suitably sized areas of glass are available for ion microprobe analysis. Furthermore, it is helpful to avoid crystallization of other volatile-bearing phases (e.g., amphibole), which could complicate analysis of the partitioning behavior of volatiles between apatite and melt.

### Experimental starting materials

We used two sets of synthetic starting materials (“BA” and “BM”; Table 1), allowing us to investigate the possible compositional effects on volatile partitioning. Both starting materials are based on compositions used in previous experimental studies and were chosen to take advantage of existing phase equilibrium constraints. Composition “BA” is a haplobasaltic andesite equivalent to composition SH3 of Prowatke and Klemme (2006). This composition produced large apatite crystals in trace-element partitioning experiments at similar temperatures and pressures (Prowatke and Klemme 2006) and enabled us to consider volatile partitioning in a simplified, Fe-free system in the first instance. Composition “BM” is a trachyte equivalent to the natural “ZAC” obsidian composition from Campi Flegrei, Naples, Italy (Fabbriozzi and Carroll 2008). The nominal compositions of both starting materials are given in Table 1.

Starting materials were prepared as mechanical mixtures of reagent grade oxides ( $\text{Al}_2\text{O}_3$ ,  $\text{SiO}_2$ ,  $\text{MgO}$ ,  $\text{MnO}$ ,  $\text{FeO}$ ,  $\text{Fe}_2\text{O}_3$ ,  $\text{TiO}_2$ ) and carbonates ( $\text{Na}_2\text{CO}_3$ ,  $\text{K}_2\text{CO}_3$ ,  $\text{CaCO}_3$ ), subsequently doped with varying amounts of phosphate [added as  $\text{Ca}_3(\text{PO}_4)_2$ ] and volatiles (added as described below). Prior to mixing, all components were dried overnight at 100 °C; the oxide powders  $\text{SiO}_2$ ,  $\text{Al}_2\text{O}_3$ ,  $\text{MgO}$ , and  $\text{TiO}_2$  were additionally fired at 1000 °C to drive off residual moisture. Dried components were then mixed in the desired proportions, ground under ethanol to produce homogenous powders, and slowly decarbonated in a box furnace (600 to 1000 °C over 6 h). For starting material “BA,” four such powders were produced: a P-bearing split doped with ~25%  $\text{Ca}_3(\text{PO}_4)_2$ ; a P-free split equivalent to that reported in Table 1, but with added Ca; and carbonated equivalents of both the P-free and P-bearing splits. Calcium was added to the P-free splits such that all splits had equal bulk CaO contents. In the case of C-bearing splits, the carbonate component was added following the decarbonation step. In this way, the bulk proportions of P and C in each run were varied by varying the proportions of the different splits added to each capsule. F and Cl were added directly to each capsule as Ca-, K-, or Na-fluorides and chlorides. Because the quantity of F and Cl added was small (typically <1 wt%), these additions did not significantly affect the proportions of the other components. Hydrogen, where present, was added as liquid water as described below.

Starting material “BM” was prepared as above, but with an additional glassing

step following decarbonation: splits were heated to 1400 °C for 30 min in a gas mixing furnace, then ground dry to homogenize. The gas mixture was held near Ni–NiO buffer conditions at the furnace temperature. This heating and grinding process was repeated 1–3 times for each split. Fluorides and chlorides were added to prior to glassing, with carbonate added afterward as above, and splits were mixed to yield the desired bulk volatile proportions (excepting water) before being added to each capsule. These additional steps were employed to ensure the thorough homogenization of starting materials as needed to aid apatite growth and equilibration in a companion study at lower experimental temperatures and pressures. As we observe no systematic textural differences between the apatites produced by the BA and BM starting materials, we assume that the starting powders were sufficiently homogenized during equilibration at high temperatures to negate any potential differences owing to the different preparations of the two starting materials.

### Piston-cylinder experiments

Starting powders were loaded into 3 mm diameter Pt capsules. In water-bearing experiments, distilled, deionized water was first added to the base of each capsule using a micro-syringe. Capsules were welded shut, then pressed into cylinders approximately 4 mm in length, and placed into 4 mm diameter outer Pt capsules containing identical proportions of starting powders  $\pm \text{H}_2\text{O}$ . The outer capsule was then welded shut and pressed into a cylindrical shape approximately 7–8 mm in length. Pressing of inner and outer capsules helped to ensure an even distribution of surrounding materials in the nested assembly. The double-capsule technique employed is essential when using Pt capsules, to reduce gradients in the chemical potentials of H and C adjacent to the sample, and thus limit the rate of  $\text{H}_2$  and C exchange between the sample and the apparatus (Hall et al. 2004; Brooker et al. 1998). In lieu of a solid buffer, this method also helps to maintain a fixed  $f_{\text{O}_2}$  (or  $f_{\text{H}_2}$ ) in the inner capsule and helps to minimize volatile loss or gain during runs. After each welding step (inner and outer capsule), capsules were weighed to check for water loss, then heated and reweighed to ensure the integrity of the weld seal.

All experiments were run in end-loaded piston-cylinder apparatus (Boyd and England 1960) at the University of Bristol. A conventional  $\frac{1}{2}$  inch diameter vessel and piston was used for runs at 1 GPa. A  $\frac{3}{4}$  inch diameter vessel was used for two runs at lower pressure (0.5 GPa). The complete sample assembly consisted of the 4 mm diameter outer Pt capsule surrounded by crushable  $\text{MgO}$  ( $\frac{1}{2}$  inch diameter setup; for the geometry of this setup, see McDade et al. 2002, their Fig. 1d) or  $\text{Al}_2\text{O}_3$  ( $\frac{3}{4}$  inch diameter setup; for the geometry of this setup, see McDade et al. 2002, their Fig. 1e) spacers positioned to center the capsule in the hot spot of the graphite furnace. The furnace + capsule assembly was fitted within a Pyrex sheath and an outer NaCl ( $\frac{1}{2}$  inch) or talc ( $\frac{3}{4}$  inch) sleeve. Loaded assemblies were then heated and pressurized according to a “hot piston in” routine. After applying an initial pressure load, the assembly was allowed to settle for at least 20 min. Temperature and pressure were then increased simultaneously, with the final pressure applied upon reaching the run temperature. This routine is in keeping with that used to determine the talc- and salt-pyrex friction correction for set pressures (~3%, McDade et al. 2002). Pressure was maintained by means of an automated pressure regulator to within  $\pm 1$  psi of the target run pressure, yielding pressure variations of <<1% relative. Run temperature was monitored using  $\text{W}_{97}\text{Re}_{3}$ – $\text{W}_{75}\text{Re}_{25}$  (D-type) thermocouples, inserted along the assembly axis adjacent to the top of the charge. Temperature was maintained by automated adjustment of the operating power via a Eurotherm, with typical deviations from target of <1 °C. No attempt was made to correct temperatures for a pressure-dependence of e.m.f., although this effect is generally considered negligible for the type of thermocouple used here (Brooker and Kjarsgaard 2011).

To encourage growth of experimental apatites, runs were first heated to super-liquidus temperatures (1450–1500 °C), and then cooled at a constant rate to a terminal temperature of 1250 °C, following Prowatke and Klemme (2006). Super-liquidus heating reduces the availability of nuclei and/or secondary nucleation sites for crystallizing phases, fostering the growth of fewer, larger crystals. A slow cooling ramp results in lower degrees of undercooling and thus further favors crystal growth over nucleation (e.g., Swanson 1977). Typical cooling rates were 20 or 50 °C/h, depending on the bulk water content. Even lower cooling rates ( $\leq 10$  °C/h) were applied to some runs with lower bulk phosphate contents or nominally zero bulk OH contents (Table 2). Samples were then allowed to equilibrate at the final run temperature, during which time a small temperature cycle was applied ( $\pm 10$  °C at 1 °C/min) to enhance crystal growth (e.g., Mills and Glazner 2013). Total run times ranged from 20–24 h and were chosen to provide sufficient time for crystal-melt equilibration, as evidenced by experiments at similar conditions (Prowatke and Klemme 2006), while minimizing the time available for diffusive exchange at high temperatures. At the end of each run, charges were quenched isobarically by cutting the operating power while manually maintaining the terminal run pressure.

**TABLE 1.** Target compositions for starting materials

	BA (SH3)	BM (ZAC)
	Prowatke and Klemme (2006)	Fabbriozzi and Carroll (2008)
$\text{SiO}_2$	53.50	62.20
$\text{TiO}_2$		0.45
$\text{Al}_2\text{O}_3$	17.70	18.71
$\text{FeO}$		3.19
$\text{MgO}$	11.80	0.23
$\text{MnO}$		0.27
$\text{CaO}$	12.40	1.65
$\text{Na}_2\text{O}$	2.80	6.16
$\text{K}_2\text{O}$	1.80	7.14
Total	100.00	100.00

TABLE 2. Experimental run conditions

Run	Starting material(s)	Nominal bulk volatile contents added							P (GPa)	T init (°C)	T final (°C)	Cooling rate (°C/h)	Initial dwell time (min)	Cooling time (h)	Final dwell time (min)	Phases present
		Ca <sub>3</sub> (PO <sub>4</sub> ) <sub>2</sub> added (wt%)	H <sub>2</sub> O (wt%)	CO <sub>2</sub> (wt%)	F (wt%)	Cl (wt%)	F source	Cl source								
BA1	SH3	25	5						1	1450	1250	50	104	4	15	gl + ap ± cpx
BA2	SH3/SH3C	25	3	0.2					1	1450	1250	50	74	4	16	gl + ap ± ?cpx
BA4	SH3/SH3C	25	1	0.4					1	1500	1250	20	60	12.5	11	gl + ap
BA7	SH3/SH3C	25		0.5					1	1500	1250	10	120	25	15	gl + ap
BA13	SH3 (glassed)	25	5						1	1450	1250	50	120	4	15	gl + ap
BA16	SH3/SH3C	25	1	0.4					1	1500	1250	20	60	12.5	10	gl + ap
BA3	SH3	25	5		1		CaF <sub>2</sub>		1	1450	1250	50	120	4	15	gl + ap
BA6	SH3/SH3C	25	1	0.4	1		CaF <sub>2</sub>		1	1500	1250	20	60	12.5	12	gl + ap
BA9 (rpt)	SH3	25	5		2		1 wt% CaF <sub>2</sub> & 1 wt% KF		1	1450	1250	20	120	10	11	gl + ap
BA10	SH3/SH3C	10	1	0.4	1		CaF <sub>2</sub>		1	1500	1250	20	60	12.5	12	gl ± ap
BA11	SH3/SH3C	25	1	0.4	2		CaF <sub>2</sub>		1	1500	1250	20	60	12.5	11	gl + ap
BA15	SH3/SH3C	5	1	0.4	1		CaF <sub>2</sub>		1	1400	(1250)	4	120	32	62	gl + cpx ± ap
BA12	SH3/SH3C	25	1	0.4	1		CaF <sub>2</sub>	CaCl <sub>2</sub>	1	1500	1250	20	60	12.5	10	gl + ap
BA14	SH3	25	5		1		CaF <sub>2</sub>	CaCl <sub>2</sub>	1	1450	1250	50	120	4	17	gl + ap
BM10	BMP25	25	5						1	1450	1250	50	120	4	15	gl + ap
BM11	BMP25	25		1.0					1	1500	1250	10	1169	25	9	gl + ap <sup>a</sup>
BM12	BMP25–5000	25	1	0.5					1	1500	1250	20	60	12.5	10	gl + ap
BM13	BMP25–5000	25	1	0.5	1		NaF		1	1500	1250	20	60	12.5	9	gl + ap
BM14	BMP25–5000	25	1	0.5	1		NaF	NaCl	1	1500	1250	20	60	12.5	12	gl + ap
BM15	BMP25–5000	25	1	0.5					0.5	1500	1250	20	60	12.5	11	gl + ap <sup>b</sup>
BM16	BMP25–5000	25	1	0.5	1		NaF	NaCl	0.5	1500	1250	20	60	12.5	10	gl + ap <sup>c</sup>

<sup>a</sup> Ap skeletal/hopper forms. <sup>b</sup> Just volatile-saturated? <sup>c</sup> Just volatile-saturated.

Following quench, capsules were removed from the assembly and sectioned using a micro-saw. To preserve the double capsule assembly, it was not possible to pierce inner capsules to test for the presence of a free fluid phase, and instead we take the absence of vesicles or gas pockets in most experiments as evidence of volatile undersaturation (two “BM” samples containing minor vesicles are indicated in Table 2). Sectioned capsules were ground using abrasive SiC papers (220 to 1200 grit) and progressively polished using diamond suspensions (6, 3, and 1  $\mu\text{m}$ ). Polished capsules were then mounted either in In metal or a thin layer of EpoFix resin, with the aim of minimizing H backgrounds during subsequent ion microprobe analysis.

## ANALYTICAL METHODS

### Electron probe microanalysis

Apatite and glass major element compositions were determined by electron probe microanalysis using a Cameca SX100 5-spectrometer instrument at the University of Bristol. Glasses were analyzed using a 15 kV, 2 nA electron beam defocused to a 15  $\mu\text{m}$  spot, with Na analyzed first to minimize alkali migration (Morgan and London 1996; Humphreys et al. 2006). Apatites were analyzed using a 15 kV, 10 nA beam defocused to 10  $\mu\text{m}$  to minimize migration of halogens yet still enable accurate determination of minor elements (e.g., Goldoff et al. 2012; Stock et al. 2015; see Supplemental<sup>1</sup> methods for details of analytical protocol). Calibration standards were albite for Na and Si; St. Johns olivine for Mg; sanidine for Al and K; Durango apatite for P; wollastonite or Durango apatite for Ca; ilmenite for Ti and Fe; Mn metal for Mn; MgF<sub>2</sub> for F; and NaCl for Cl. Count times were 30 s on peak for all elements except Fe and Mn (60 s on peak) and Cl and F (120 s on peak). Resulting detection limits for volatile elements in apatite were typically ~120 ppm for Cl and ~500 ppm for F, whereas in glass the detection limits were typically ~300 ppm for Cl and ~900 ppm for F (for full analytical conditions see Supplemental<sup>1</sup> materials). Raw data were processed using a PAP matrix correction scheme. Accuracy and precision of the analytical setup were monitored by repeated analysis of well-characterized secondary standards (KN18, BCR2, and synthetic F-bearing haplobasalt for glasses; oriented Durango and Wilberforce apatite crystals for apatite).

### Secondary ion mass spectrometry

Volatile compositions of apatite and coexisting glass were determined by secondary ion mass spectrometry using a Cameca ims-4f instrument at the NERC ion microprobe facility at the University of Edinburgh. The instrument is run utilizing Charles Evans and Associates PXT interface and software.

For apatite, a 5 nA <sup>16</sup>O<sup>+</sup> primary beam with a net impact energy of 14.5 keV was accelerated onto the sample. An energy window of 75 ± 20 V was applied. The spot size was ~15–20  $\mu\text{m}$ . A circular field aperture with an effective radius of 8  $\mu\text{m}$  was used to lower H and C backgrounds coming from the edge of the sputtering pit. Backgrounds were monitored using either end-member (H-free) apatites from Schettler et al. (2011) or a piece of quartz embedded within each sample mount.

In addition, a 4 min pre-sputter period at a raster size of 20  $\mu\text{m}$  was employed to minimize contamination from the sample surface. The secondary ions <sup>1</sup>H<sup>+</sup>, <sup>12</sup>C<sup>+</sup>, <sup>25</sup>Mg<sup>2+</sup>, <sup>19</sup>F<sup>+</sup>, <sup>23</sup>Na<sup>+</sup>, <sup>26</sup>Mg<sup>+</sup>, <sup>30</sup>Si<sup>+</sup>, <sup>31</sup>P<sup>+</sup>, <sup>35</sup>Cl<sup>+</sup>, <sup>39</sup>K<sup>+</sup>, and <sup>44</sup>Ca<sup>+</sup> were collected for 5, 10, 6, 10, 2, 5, 2, 2, 10, 3, and 2 s, respectively, for each 6 cycles of the magnet. Only H<sub>2</sub>O, CO<sub>2</sub>, F, P<sub>2</sub>O<sub>5</sub>, and Cl were quantified. Other elements were used to monitor for contamination with the silicate glass. The OH and CO<sub>3</sub><sup>2-</sup> contents of apatite were determined using daily working curves of <sup>1</sup>H/<sup>44</sup>Ca vs. OH and <sup>12</sup>C/<sup>44</sup>Ca vs. C acquired for a suite of natural apatite standards (Supplemental<sup>1</sup> materials), after correction for isobaric interference by <sup>24</sup>Mg<sup>2+</sup> on <sup>12</sup>C (correction generally <5%, except in the



most C-poor samples up to 15%). The same approach was taken for both F and Cl, with 95% prediction intervals calculated for every calibration line (Supplemental<sup>1</sup> materials). For a small subset of apatite crystals (<15  $\mu\text{m}$  in smallest dimension), the beam current was reduced to 2 nA resulting in a spot size of <10  $\mu\text{m}$ . This process reduced the number of ions counted, but had no appreciable effect on the calibration curve slopes. Halogens were also quantified for halogen-free experiments as a check for contamination. No effect of apatite orientation (parallel vs. perpendicular to the c-axis) on working curves for  $\text{H}_2\text{O}$ ,  $\text{CO}_2$ , F, and Cl was detected, consistent with the findings of Stock et al. (2015).

For the glass, a similar analytical setup and procedures were used as for apatite, apart from using a  $50 \pm 20$  V energy window for C analysis (a  $75 \pm 20$  V energy window was used for analysis of H and other elements). To ensure accurate determination of C contents in the Mg-rich glass, an initial set of analyses was collected at sufficient mass resolution to separate the  $^{12}\text{C}^+$  and  $^{24}\text{Mg}^{2+}$  peaks, with secondary ions collected at  $^{24}\text{Mg}^{2+}$ ,  $^{12}\text{C}^+$ ,  $^{26}\text{Mg}^+$ , and  $^{30}\text{Si}^+$  for 5, 10, 3, and 2 s, respectively, for each of 10 cycles of the magnet. In a second set of analyses on the same spot (with a 2 min pre-sputter period and 20  $\mu\text{m}$  raster), the secondary ions  $^1\text{H}^+$ ,  $^{11}\text{B}^+$ ,  $^{19}\text{F}^+$ ,  $^{26}\text{Mg}^+$ ,  $^{30}\text{Si}^+$ , and  $^{35}\text{Cl}^+$  were collected for 3, 3, 6, 2, 2, and 6 s, respectively (over 10 magnet cycles.). As with apatite,  $\text{H}_2\text{O}$  and  $\text{CO}_2$  contents of the glasses were determined using daily working curves of  $^1\text{H}/^{28}\text{Si}$  vs.  $\text{H}_2\text{O}$  and  $^{12}\text{C}/^{28}\text{Si}$  vs.  $\text{CO}_2$ , respectively, generated from standard glasses including basalts and phonolites. The calibration glasses included samples from Shishkina et al. (2010), Hauri et al. (2002), Mangan and Sisson (2000), and Brooker et al. (1999) (see Supplemental<sup>1</sup> materials for details). A field aperture was used to reduce backgrounds for H and C, which were monitored using either a volatile-free glass from Shishkina et al. (2010) or a piece of quartz embedded within each sample mount. Halogens were calculated using Lipari glass (Hunt and Hill 1993) as the primary calibration standard for Cl, and NIST SRM610 glass as the primary calibration standard for F. Halogens were also quantified for halogen-free experiments as a check for possible contamination. Values were checked against internal secondary glass standards and synthetic halogen-rich glasses synthesized using the starting material SH3. SIMS glass halogen concentrations were also checked and compared against EPMA.

## Secondary electron microscopy (SEM)

Backscattered SEM images of polished, mounted samples were collected using a Hitachi S-3500N scanning electron microscope at the University of Bristol, with a 15–20 kV accelerating voltage and 15 mm working distance. All samples were imaged prior to SIMS analysis to identify the phases present, produce image maps for sample navigation, and locate areas of apatite and glass suitable for ion microprobe work (sufficiently large and free from cracks and inclusions). To avoid contaminating the sample surface with C in advance of SIMS analysis, samples were not C coated prior to imaging in low vacuum mode. Run products were imaged again following ion microprobe work to confirm the location of sputter craters.

## Apatite stoichiometry

We followed the calculation scheme of Ketcham (2015) for stoichiometric calculations, with formula proportions calculated on a 25-oxygen basis. We placed Mg, Mn, Fe, and Na on the Ca site, and Si onto the phosphate site. Any deficiency in P on the phosphate site was filled with carbonate where possible; any remaining carbonate was placed onto the channel volatile site together with F, Cl, and hydroxyl (Supplemental<sup>1</sup> Table 1). Stoichiometric totals are generally good, with the Ca-site contents  $9.967 \pm 0.070$ , P-site contents  $6.037 \pm 0.030$ , and average X-site totals for the halogen-bearing experiments of  $1.913 \pm 0.087$  (Supplemental<sup>1</sup> Table 1), although halogen-free experiments have lower totals (see below). There is also a correlation between the measured OH and OH calculated by difference (see later discussion).

## RESULTS

### Experimental run products

Experimental run products for both starting materials typically comprise microlite-free glass + apatite, with a minority of samples also containing clinopyroxene  $\pm$  fluid (see Table 2; Fig. 1). The experiments were designed to be volatile-undersaturated, because of the difficulty of constraining the composition of any fluid(s). The two experiments run at 0.5 GPa contain sparse vesicles, which may indicate that these samples had just reached volatile saturation. Apatites are large and euhedral (typically up to 100  $\mu\text{m}$  perpendicular to c-axis and up to 1 mm parallel to the

c-axis) and commonly contain melt inclusions that are visible in sections cut perpendicular to the c-axis (Fig. 1). Experiments run at lower pressures or higher cooling rates formed apatites with more skeletal or hopper textures.

**Glasses.** Experimental glasses from the “BA” experiments are Al-rich haplobasalts with  $\sim 5$  wt% total alkalis, 9–10 wt%  $\text{MgO}$ , 14–16 wt%  $\text{Al}_2\text{O}_3$ , and 18–30 wt%  $\text{CaO}$  on an anhydrous basis (Supplemental<sup>1</sup> Table 2). Silica contents are 44.4–49.6 wt%  $\text{SiO}_2$ , normalized to 100% on an H- and C-free basis. The glasses have high volatile concentrations, as expected given the experimental run pressure of 1 GPa and nominal bulk volatile compositions (Table 2). Some  $\text{CO}_2$  was found even in the nominally C-free runs, which we attribute to infiltration of C through the Pt capsule walls during the course of the experiment (Brooker et al. 1998) or possibly incomplete decarbonation of the starting material and/or atmospheric contamination.  $\text{H}_2\text{O}$  contents are in the range 0.7–7.1 wt%, and  $\text{CO}_2$  concentrations range from 300 ppm to 1.3 wt% (Supplemental<sup>1</sup> Table 2). Halogen concentrations in the glass are 0.8–1.6 wt% F and  $\sim 0.8$  wt% Cl (Supplemental<sup>1</sup> Table 2).

The “BM” experiments formed phonolitic glasses with 57.2–61.8 wt%  $\text{SiO}_2$  and 12.6–16.3 wt% total alkalis (Supplemental<sup>1</sup> Table 2). For the halogen-bearing “BM” experiments, halogens were added in the form of NaCl and NaF, so the melts for these experiments have correspondingly higher  $\text{Na}_2\text{O}$  contents (Supplemental<sup>1</sup> Table 2).  $\text{H}_2\text{O}$  concentrations are in the range 1.3–7.1 wt% and  $\text{CO}_2$  concentrations are 1600–7100 ppm, consistent with volatile concentrations in the BA experimental glasses. Fluorine contents are also similar to those in the BA glasses (0.85–1.0 wt% F) but Cl concentrations are higher (1.25 wt% Cl) for the same nominal bulk Cl added. Glasses are homogeneous throughout each sample, with typical relative standard deviations of approximately 1.2% for  $\text{CO}_2$ ,  $\text{H}_2\text{O}$ , F, and Cl. This is smaller than the analytical uncertainty, and we therefore used the analytical uncertainty to estimate and propagate errors in the partitioning data.

**Apatites.** Experimental apatites from the halogen-free BA experiments are hydroxy-apatites with 0.7–1.7 wt%  $\text{H}_2\text{O}$  and a wide range of C contents up to 1.80 wt% (C expressed as  $\text{CO}_2$ ) (Supplemental<sup>1</sup> Table 1). Apatites from the halogen-bearing experiments are hydroxyl-bearing fluor-apatite, with  $\geq 2$  wt% F and com-

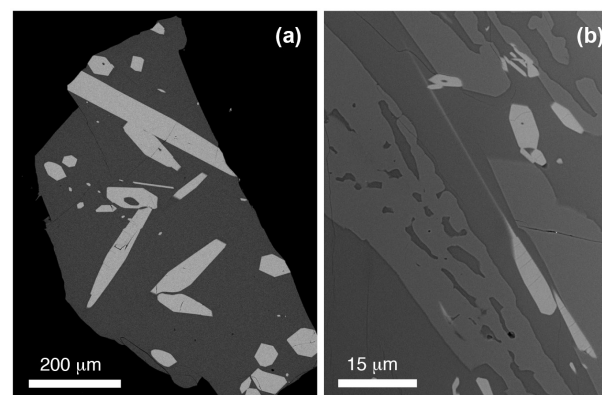


**FIGURE 1.** Experimental run products from BA experiments showing glass-rich materials and large, euhedral apatite crystals. (a) BA1 (H-C). (b) BA15 (HCFCl), the most strongly crystallized experiment containing glass + clinopyroxene + apatite.

positions systematically shifted to lower OH and C contents ( $\leq 0.8$  wt% H<sub>2</sub>O and  $\leq 0.22$  wt% CO<sub>2</sub>, Supplemental<sup>1</sup> Table 1). Apatites from these halogen-bearing experiments have volatile contents of  $F > Cl \gg OH > C$ , even when these components were added in the same concentrations to the starting mixture (e.g., BA12, which had 1 wt% each of F, Cl, and OH in the starting material, Tables 2 and Supplemental<sup>1</sup> Table 1). In the halogen-free experiments, the apatite H<sub>2</sub>O and CO<sub>2</sub> contents increase with increasing dissolved H<sub>2</sub>O and CO<sub>2</sub> in the coexisting glass, respectively, and the CO<sub>2</sub> content increases with increasing CO<sub>2</sub>/(H<sub>2</sub>O+CO<sub>2</sub>) in the glass (Fig. 2). The same pattern is observed in the halogen-bearing experiments, but with lower overall OH and C contents as described above. Similarly, experimental apatites from the BM experiments show high H<sub>2</sub>O and CO<sub>2</sub> contents in the halogen-free runs, (0.7–1.2 wt% H<sub>2</sub>O and up to 1.2 wt% CO<sub>2</sub>) and significantly lower concentrations in the halogen-bearing experiments, which routinely produced fluor-apatite with  $>2.5$  wt% F (Supplemental<sup>1</sup> Table 1). Carbon contents increase with increasing concentration of the minor elements (Mg, Na, and Si; Fig. 3).

The stoichiometry calculations suggest that, for the halogen-free experiments, there is no space on the phosphate site for carbonate, such that all the carbonate and hydroxyl are accommodated on the channel site (Supplemental<sup>1</sup> Table 1). In contrast, for some of the halogen-bearing experiments, there is sufficient space on the phosphate site to assign some of the carbonate, with the channel site occupied by the remaining carbonate, halogens, and hydroxyl.

Minor element concentrations in the apatites are clearly related to the host melt composition. Apatites from the BM experiments typically contain higher alkalis and lower Mg compared with those from the BA experiments (Supplemental<sup>1</sup> Table 1).

### Partitioning data

We used the experimental apatite and glass compositions to calculate the apparent Nernst partition coefficients,  $D_i = (C_i^{ap}/C_i^m)$  where  $C$  is the concentration of element  $i$  in wt%. This representation allows the distribution of volatile species between apatite and melt to be directly compared with other literature data (in the case of H, F, and Cl), and to give the first experimentally determined

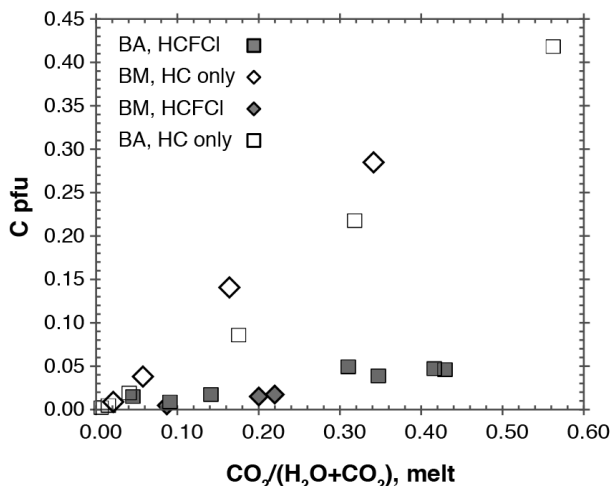


FIGURE 2. Apatite CO<sub>3</sub><sup>2-</sup> content, expressed as apfu (ions per formula unit) as a function of the CO<sub>2</sub>:H<sub>2</sub>O ratio of the host melt.

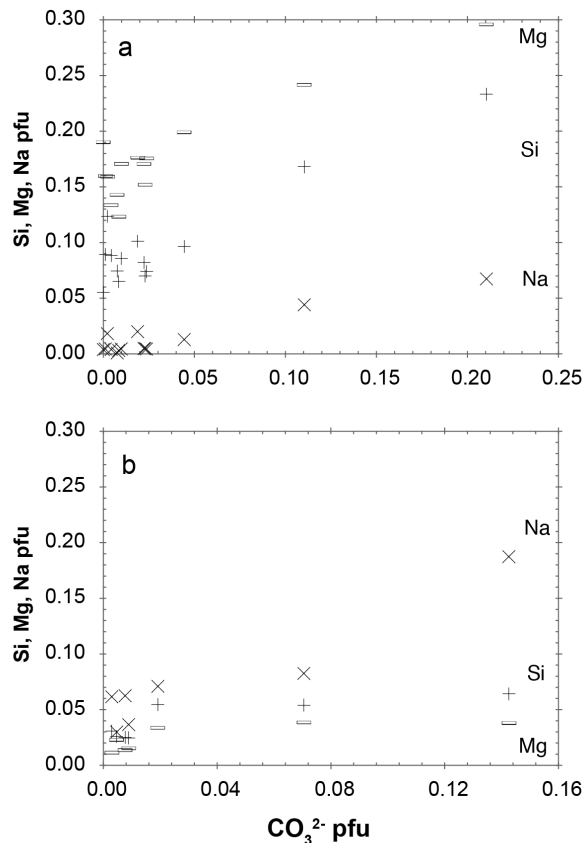


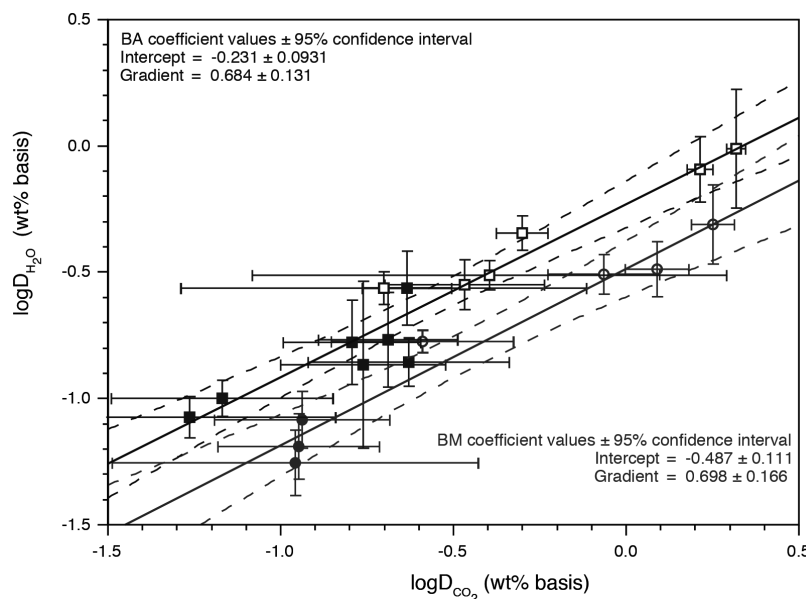
FIGURE 3. Apatite carbonate concentrations increase systematically with Mg, Si, and Na contents in apatite. Minor element concentrations, overall, reflect the composition of the host melt. (a) “BA” haplobasaltic andesite experiments. (b) “BM” Breccia Museo (trachyte) experiments.

partitioning data for C between apatite and silicate melts. Note that to maintain consistency with previous studies (e.g., McCubbin et al. 2015), we have calculated the partition coefficients between volatile abundances in apatite and melt as the same species, i.e., OH in apatite is calculated as the equivalent H<sub>2</sub>O content, whereas CO<sub>3</sub><sup>2-</sup> in apatite is calculated as the equivalent CO<sub>2</sub> content, on a concentration (wt%) basis. Our calculated  $D$  values show, as expected, that F is highly compatible in apatite, with  $D_F$  between 1.3 and 3.6 (average = 2.2). Chlorine is moderately compatible ( $D_{Cl} = 0.6$  to 2.3), and OH is generally incompatible ( $D_{OH} = 0.06$  to 0.97; average = 0.27) (Supplemental<sup>1</sup> Table 3), although its compatibility varies with a bulk mixed volatile content.  $D_{CO_3^{2-}}$  is variable, with values ranging from 0.05 to 2.1. Notably, CO<sub>3</sub><sup>2-</sup> was actually compatible in apatite in several of the halogen-free experiments. Both  $D_{CO_3^{2-}}$  and  $D_{OH}$  are significantly higher in the halogen-free runs.

Although Nernst partition coefficients ( $D$ ) have been widely reported in studies of volatile partitioning in apatite, the more appropriate measure of partitioning for major chemical components competing for the same crystallographic site—such as F, Cl, and OH in apatite—is the exchange coefficient,  $K_D$  (e.g., Roeder and Emslie 1970), defined as the ratio of partition coefficients of two species, e.g.:

$$K_D^{OH-Cl} = (OH_{ap}/OH_m)/(Cl_{ap}/Cl_m) = (OH_{ap}/Cl_{ap})/(OH_m/Cl_m) \quad (1)$$

**FIGURE 4.** Partitioning data for H-C exchange between apatite and melt, calculated on the basis of wt% CO<sub>2</sub> and H<sub>2</sub>O in both phases. Circles: “BM” (trachyte) series; squares: “BA” (haplobasaltic andesite) series. Open symbols are halogen-free experiments. Closed symbols are halogen-bearing experiments. Solid line = best fit; short-dashed line = 95% confidence limits on the fit. Uncertainties on individual data points represent accuracy based on 95% prediction intervals from SIMS working curves (and are much larger than the precision, which is very good).



According to the strict definition of these distribution coefficients, the volatile components should be calculated using activity (or mole fraction if assuming ideal behavior). However, it is not obvious that this approach brings greater clarity to the results of these experiments. In particular, the high pressures and range of melt compositions used means that there is some considerable uncertainty concerning the validity of models describing the distribution of dissolved water and C species in the melt (e.g., Brooker et al. 1999; Sowerby and Keppler 1999; Morizet et al. 2002; Hui et al. 2008), even if the apatite behavior is ideal at high pressure and temperature (see Li and Hermann 2017 for a discussion). For completeness, we give apatite-melt  $K_D^{OH-Cl}$ ,  $K_D^{OH-F}$ , and  $K_D^{Cl-F}$  in mole fraction form (Supplemental<sup>1</sup> materials) using the same water speciation model as Li and Hermann (2017) for consistency with their approach, though this may not be the most appropriate for the range of melt compositions included. These  $K_D$  values are calculated by normalizing the volatile site contents such that  $XOH + XF + XCl = 1$ , excluding carbonate (Supplemental<sup>1</sup> materials). For OH-carbonate exchange, however, we present only  $K_D$  values calculated on a concentration basis to avoid introducing errors as a result of the poorly understood variation in C speciation in silicate melts (e.g., Morizet et al. 2002).

From our experiments, the resulting distribution coefficients (calculated following McCubbin et al. 2015 as the ratio of partition coefficients) are  $K_D^{H_2O-F} = 0.023\text{--}0.09$ ,  $K_D^{H_2O-Cl} = 0.07\text{--}0.11$ , and  $K_D^{Cl-F} = 0.27\text{--}0.98$  (Supplemental<sup>1</sup> Table 3). Apatite-melt distribution coefficients for H<sub>2</sub>O–CO<sub>2</sub> exchange are defined more rigorously in Figure 4 through  $\log K_D^{H_2O-CO_2} = \log D_{H_2O} - \log D_{CO_2}$ , where  $\log K_D$  is the intercept. This gives  $K_D^{H_2O-CO_2} = 0.355 \pm 0.05$  for the “BM” experiments and  $0.629 \pm 0.08$  for the “BA” experiments (uncertainties represent a 95% prediction interval). This suggests a dependence on the melt major element composition, with systematically higher  $K_D$  values (as calculated for individual experiments) in the BM system (Fig. 4). The gradient in Figure 4 is approximately 0.65 for both the BM and BA experiments, whereas for an ideal system it should be equal to 1.0. This suggests that C–H partitioning may be non-ideal

for high-temperature igneous apatites, which would be consistent with the development of significant vacancy concentrations in the more carbonate-rich apatites (see below).

## DISCUSSION

### CO<sub>3</sub><sup>2-</sup> in apatite

Our primary focus was to define the carbonate partitioning behavior between hydroxyl-bearing apatite and hydrous silicate melt. The apatites themselves contain quite high carbonate concentrations, typically several hundred to a few thousand parts per million, even in the halogen-bearing experiments. This is in contrast with natural silicate melts, which commonly record magmatic volatile concentrations only after significant degassing of CO<sub>2</sub>, either into a fluid phase or during post-entrapment modification and formation of a shrinkage bubble, resulting in lower CO<sub>2</sub> contents of typically a few hundred parts per million (Wallace 2005; Blundy et al. 2010; Hudgins et al. 2015; Tuohy et al. 2016; MacLennan 2017). The  $K_D$  values for OH-carbonate exchange ( $K_D^{H_2O-CO_2}$ ) appear to be dependent on the melt major element composition, with higher values in the BM experiments than in the BA experiments (see Fig. 4; Supplemental<sup>1</sup> Table 3). In contrast, the apparent carbonate-halogen exchange coefficients are very low, with  $K_D^{CO_2-Cl} < 0.17$  and  $K_D^{CO_2-F} < 0.11$  (Supplemental<sup>1</sup> Table 3). To the best of our knowledge, these are the first experimental constraints on carbonate partitioning in igneous apatite, so we are unable to compare our data with those of other studies. The advantage of SIMS analysis is that the total C concentration is technically easy to measure in situ on unoriented grains, although it cannot provide structural information related to site occupancy, which requires techniques such as FTIR, XRD, or NMR (e.g., Fleet 2017).

### Incorporation of CO<sub>3</sub><sup>2-</sup> in experimental igneous apatites

Previous work has identified that carbonate can be accommodated in apatite via two key substitution mechanisms. In “Type A” apatite, carbonate is incorporated by exchange of a hydroxyl ion

for a carbonate anion within the c-axis channel site, plus an OH<sup>-</sup> vacancy for charge compensation (e.g., LeGeros et al. 1969; Bonel 1972; Young et al. 1981):



In “Type B” carbonate, the CO<sub>3</sub><sup>2-</sup> ion is substituted for PO<sub>4</sub><sup>3-</sup>, as demonstrated by substantially lower P concentrations in carbonate-apatite. This substitution may be charge-balanced according to the mechanism



(e.g., Binder and Troll 1989), although NMR work shows that the charge-balancing F<sup>-</sup> is not directly interacting with carbonate as a tetrahedral complex (Mason et al. 2009). Various other substitution mechanisms are also possible (e.g., Pan and Fleet 2002):



Apatite data from our halogen-free experiments indicate that the Type A substitution mechanism is the dominant one for the carbonate anion. Both the carbonate and OH contents of apatite vary systematically with increasing CO<sub>2</sub>/(H<sub>2</sub>O+CO<sub>2</sub>) in the host melt (see Fig. 2). This indicates that the apatite carbonate concentrations are directly linked to the volatile composition of the melt. Since OH is well known to occupy the channel site, this indicates that carbonate is also incorporated into the channel site. The stoichiometry calculations also indicate that there is insufficient space on the phosphate site to accommodate any significant Type B carbonate, and therefore the carbonate should sit on the X-site (Type A; see Supplemental<sup>1</sup> Table 1). This has been confirmed using FTIR (see Supplemental<sup>1</sup> Fig. 1) where the positions of the carbonate ν<sub>3</sub> vibrational peaks are consistent with dominantly A-site occupation (e.g., Fleet et al. 2004; Fleet 2017). However, while OH calculated by charge balance in the channel site is equivalent to measured OH in the most OH-rich samples, for samples with higher carbonate contents the measured OH is significantly lower than OH calculated by charge balance (Fig. 5). This suggests that the incorporation of carbonate into igneous apatite at high temperatures may involve the creation of vacancies, significantly greater than the number of OH<sup>-</sup> vacancies predicted to charge balance CO<sub>3</sub><sup>2-</sup> via Equation 2. The presence of structural H<sub>2</sub>O in the channel site (e.g., Mason et al. 2009; Yoder et al. 2012) seems unlikely given the high run temperatures of the experiments.

In fact, the under-occupancy of the X-site suggests the formation of a significant “oxyapatite” component, with O<sup>2-</sup> (and a vacancy) substituting for 2OH<sup>-</sup> within the channel site (Trombe and Montel 1978; Young et al. 1981; Schettler et al. 2011). First-principles calculations support the idea that significant defects on the channel site can be formed at high temperatures (>1000 K), including the formation of oxyapatite coupled to OH<sup>-</sup> vacancies, resulting in significant non-stoichiometry at high temperatures (Matsunaga and Kuwabara 2007; Kubota et al. 2014). This deviation from stoichiometric mineral formulas is consistent with our interpretation that C-H exchange is non-ideal.

Our observations are also consistent with experiments that

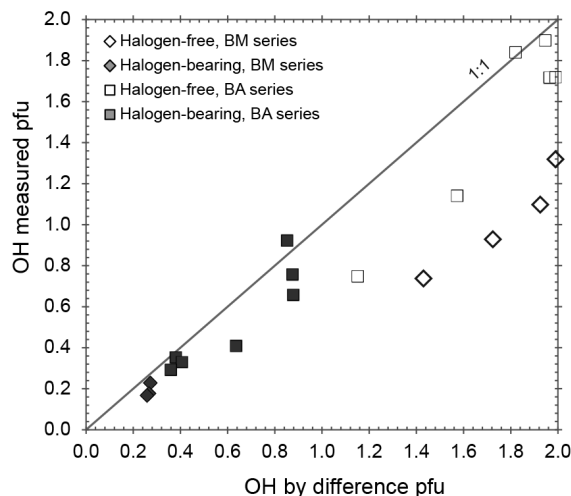


**FIGURE 5.** Comparison of measured OH contents (pfu) with OH “by difference” from the sum of the volatile site. Apatite from halogen-bearing experiments (filled symbols) and from halogen-free experiments, but with low carbonate contents, show reasonably good correspondence, whereas the carbonate-rich apatites show a significantly lower measured OH content, indicating the presence of vacancies.

resulted in the formation of Type A carbonate apatite by the reaction of hydroxyapatite with dry CO<sub>2</sub> (Bonel 1972); and with first-principles calculations that indicate a greater stability of the Type A substitution at high temperatures (Kubota et al. 2014). The lack of negative correlation between CO<sub>3</sub><sup>2-</sup> and Ca or P also argues against a significant B-type substitution (De Maeyer et al. 1993). However, the highest total carbonate contents are also associated with high minor element concentrations (e.g., Mg, Na), which suggests a subsidiary Type B substitution similar to Equation 5 or 6. Peroos et al. (2006) showed that although the Type A substitution was energetically favorable, a Type B substitution, charge balanced by Na<sup>+</sup>, was also favorable when Type-A carbonate was already present.

In contrast, the stoichiometry of apatites from our halogen-bearing experiments suggests the additional formation of some B-type carbonate apatite. In some of these apatites, the phosphate site has enough space to accommodate some carbonate, and the channel site incorporates the remainder plus halogens and OH (Supplemental<sup>1</sup> Table 1). In contrast with apatites from the halogen-free experiments, there is good agreement between OH contents calculated by difference and measured OH for the halogen-bearing experiments (Fig. 5). This suggests that these calculated site assignments are reasonable, and consistent with calculations showing that at high temperatures the Type A carbonate substitution should be more stable than Type B (e.g., Kubota et al. 2014). However, we suggest that in the presence of abundant halogens, the formation of F-Cl-OH apatite is the most energetically favorable, and that carbonate can be shifted onto the phosphate site.

#### OH-Cl-F distribution between apatite and silicate melt

The OH-F-Cl apatite-melt exchange coefficients calculated from our experimental data are consistent with those of other studies, but with some significant differences. There are only two other experimental Cl-OH-F apatite-melt partitioning studies



**TABLE 3.** Summary of experimental conditions for studies included in multiple regression analysis

Reference	Bulk composition	Melt CaO (wt%)	T (°C)	P (MPa)	Apatite measured	Melt measured	Fluid measured	Volatil state
This study	Haplo-basaltic andesite	15.7–19.0	1250	1000	OH, F, Cl, C (SIMS); F, Cl (EPMA)	H <sub>2</sub> O, F, Cl, C (SIMS); F, Cl (EPMA)	n/a	Volatile-undersaturated
This study	Trachyte	2.4–3.3	1250	1000	OH, F, Cl, C (SIMS); F, Cl (EPMA)	H <sub>2</sub> O, F, Cl, C (SIMS); F, Cl (EPMA)	n/a	Volatile-undersaturated
Doherty et al. (2014)	Rhyodacite	0.4–3.1	849–947	50–52	F, Cl (EPMA)	F, Cl (EPMA)	Cl (mass balance)	Mostly volatile-saturated
Li and Hermann (2015)	Pelite	2.3–2.5	630–900	2500–4500	F, Cl (EPMA)	H <sub>2</sub> O (FTIR); F, Cl (EPMA) F, Cl (EPMA)	n/a	Volatile-undersaturated
Li and Hermann (2017)	Pelite	2.4	800	2500	F, Cl (EPMA)	H <sub>2</sub> O (mass balance); F, Cl (EPMA)	n/a	Volatile-undersaturated
Mathez and Webster (2005)	Basalt	5.3–16.9	1066–1150	200	F, Cl (EPMA)	H <sub>2</sub> O (mass balance)	Cl (chloridometer)	Mostly volatile-saturated
McCubbin et al. (2014)	Fe-rich basalt	3.8–9.0	950–1000	1000–1200	OH, F, Cl (SIMS)	H <sub>2</sub> O, F, Cl (SIMS)	n/a	Volatile-undersaturated
Potts et al. (2015)	Lunar basalt mesotaxis	8.0–9.0	1350–1450	1000	OH, F, Cl (SIMS)	H <sub>2</sub> O, F, Cl (SIMS)	n/a	Volatile-undersaturated
Webster et al. (2009)	Rhyodacite to rhyolite	0.5–2.4	900–923	198–205	F, Cl (EPMA)	F, Cl (EPMA)	Cl (chloridometer)	Volatile-saturated
Webster et al. (2017) <sup>a</sup>	High-Si rhyolite	0.1–2.1	722–1000	49–202	F, Cl (EPMA)	H <sub>2</sub> O (FTIR); F, Cl (EPMA)	Cl (chloridometer)	Volatile-saturated

<sup>a</sup> These runs typically contained <25 ppm CO<sub>2</sub> as contaminant (not studied).

with direct measurements of all channel site components. The extended abstract by Potts et al. (2015) reported experiments conducted at 1 GPa and 1350–1450 °C with a composition similar to the mesotaxis of lunar basalts, while McCubbin et al. (2015) performed apatite-melt experiments at 1–1.2 GPa and 950–1000 °C using an Fe-rich basalt. Our calculated nominal  $D_F$ ,  $D_{Cl}$ , and  $D_{OH}$  are within the range reported by these and other previous studies (Fig. 6; Table 3). This includes experiments without direct measurement of OH, for which we calculated nominal  $D_{OH}$  “by difference” (see Table 3; Doherty et al. 2014, rhyodacite at 50 MPa, 850–950 °C; Webster et al. 2009, rhyodacite at 200 MPa, ~900 °C; Mathez and Webster 2005, basalt, 1050–1150 °C; Webster et al. 2017, rhyolite at 50–200 MPa and 700–1000 °C; and Li and Hermann 2015, 2017, “pelite” melts at 2.5–4.5 GPa and 600–900 °C). This was done assuming a stoichiometric channel site containing no carbonate (see earlier discussion) and calculating  $H_2O_{(m)}$  by difference where

necessary. These “by difference” calculations are subject to a significant uncertainty (e.g., Devine et al. 1995; Humphreys et al. 2006), and the direct analysis of all volatile components in both melt and apatite is strongly encouraged for future work. The data set also includes a mixture of volatile-saturated and volatile-undersaturated experiments (see Table 3), and at least

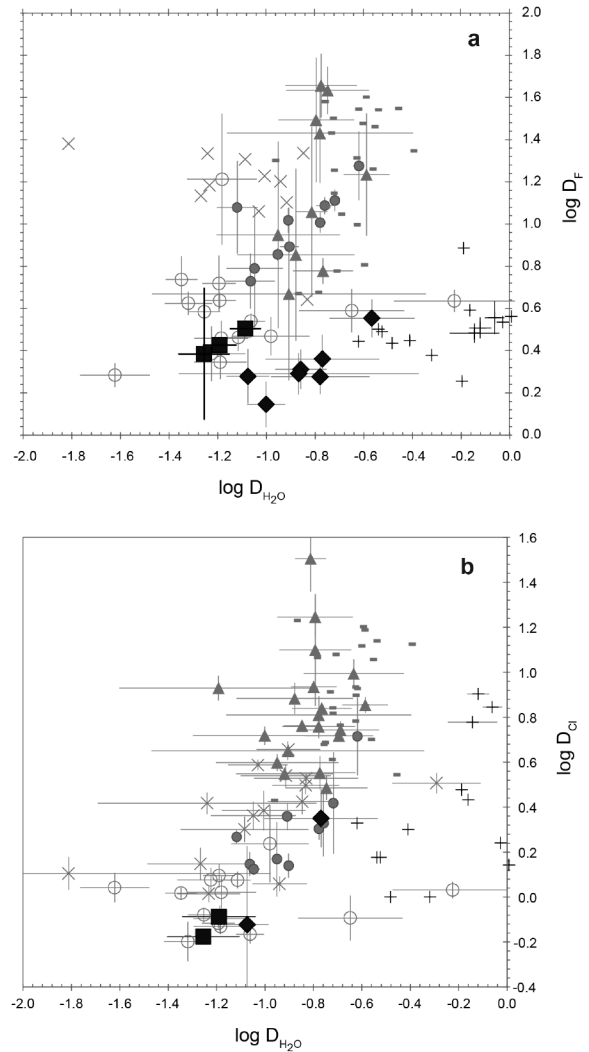


**FIGURE 6.** Nominal partition coefficients for OH, Cl, and F, from this study and from the literature, wt% basis. Gray dashes = Webster et al. (2017); gray crosses = Webster et al. (2009); gray triangles = Doherty et al. (2014); open circles = Mathez and Webster (2005); filled circles = McCubbin et al. (2015); pluses = Potts et al. (2015). Black diamonds = “BA” experiments; black squares = “BM” experiments.

some of the volatile-saturated experiments are rich enough in Cl that fluid immiscibility is likely (e.g., Webster et al. 2017). These results, perhaps not surprisingly, are strongly scattered and cover a wide compositional range (Figs. 6–8). The variation in starting materials and experimental conditions suggests that some of this variability may be due to the effects of changing melt composition or pressure and temperature. This is supported by a systematic decrease in both  $D_F$  and, to a lesser extent,  $D_{Cl}$ , with increasing temperature and increasing melt CaO content in the compiled literature data set. Increasing experimental pressure causes only a minimal decrease in  $D_{F,Cl}^{ap-m}$ .

As with Figure 4, the distribution coefficients for OH-halogen exchange are equivalent to the intercept in Figure 6. Thus, our calculated  $K_D^{OH-F}$  are slightly lower than those of Potts et al. (2015)

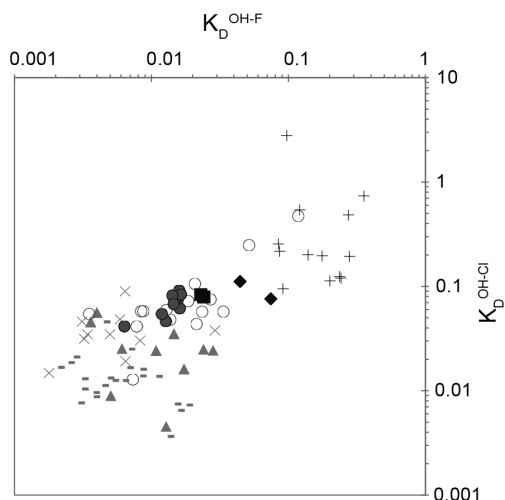


**FIGURE 7.** Experimentally derived distribution coefficients for OH-halogen exchange between apatite and silicate melt (calculated on a wt% basis), in comparison with  $K_D$  values from the literature. Symbols are the same as for Figure 6.

but higher than those of McCubbin et al. (2015). Each study was conducted at the same pressure (1 GPa), so we interpret these differences in  $K_D$  as predominantly a result of differences in temperature (in the range 950 to 1450 °C). This is borne out by the results of a multiple regression analysis of the full literature data set, including our new experiments (Fig. 8), to an equation of the form

$$\log K_D = a + b/T + c(P - 1)/T \quad (7)$$

following the approach of Piccoli and Candela (1994). This shows a clear log-linear increase in  $K_D^{\text{OH-halogen}}$  with increasing temperature, which indicates a preference for the OH end-member at higher temperatures for a given melt composition. Despite the inclusion of both volatile-saturated and volatile-undersaturated experiments from rhyolite to basalt, the relative consistency of the published  $K_D$  values, as a function of temperature, is striking, and confirms that temperature is the dominant overall control on apatite-melt volatile partitioning. The CaO content in the melt was not a significant variable, presumably due to covariation with temperature. The pressure term was of subsidiary significance and we obtained similar confidence on the parameter values when excluding the third term in Equation 2 (Table 4). For OH-Cl exchange, the results gave  $a = 1.0729 \pm 0.2353$  and  $b = -2938.4 \pm 282.3$ , whereas for OH-F exchange,  $a = 1.2590 \pm 0.2942$  and  $b = -3853.6 \pm 367.8$  (Fig. 8, Table 4).

We compared these results with earlier thermodynamic expressions derived by Piccoli and Candela (1994) for the system apatite-fluid. Their  $K_D^{\text{ap-fl}}$  were calculated using the thermodynamic data of Zhu and Sverjensky (1991) to give the fugacity ratio for the coexisting aqueous fluid, with aqueous species data derived from Robie et al. (1978) and Stull and Prophet (1971). High-temperature values for  $K_D^{\text{OH-Cl}}$  are up to an order of magnitude lower for the apatite-fluid than for the apatite-melt  $K_D$  exchange data, but there is better agreement between the two systems at low temperatures (Fig. 8). There is also agreement on the direction of change of  $K_D$  with temperature (cf. Li and Hermann 2015). In contrast, the values for  $K_D^{\text{OH-F}}$  are 2–3 orders of magnitude lower for apatite-fluid

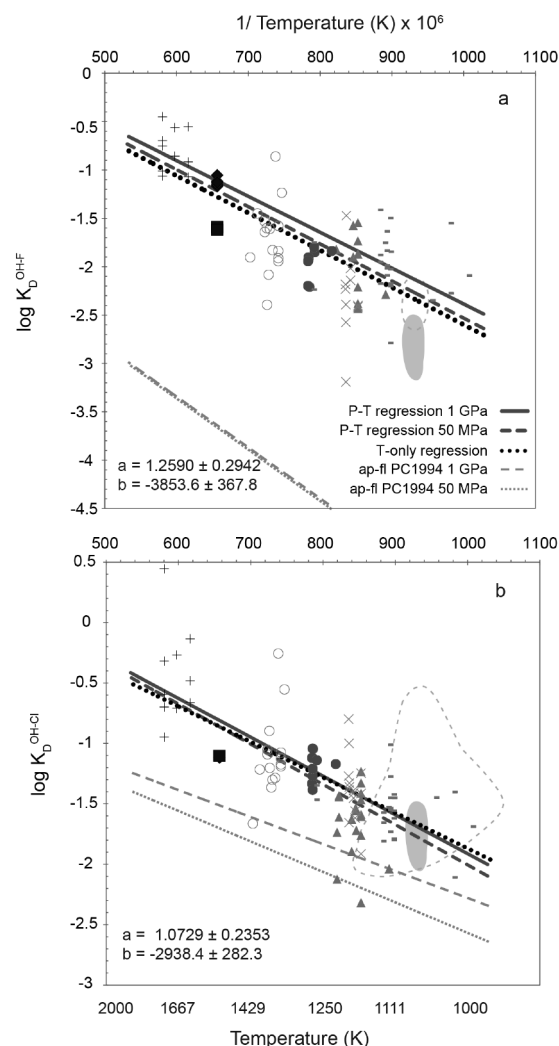


**FIGURE 8.** Regression analyses of experimentally determined halogen-OH distribution coefficients for apatite-melt (wt% basis), with dependence on both  $P$  and  $T$  [ $\log K_D = a + b/T + c(P - 1)/T$ ] or temperature only ( $\log K_D = a + b/T$ ). Regression coefficients for  $T$ -only analysis are given. Data symbols are the same as for Figure 6. Dark gray lines = predicted variations at 1 GPa (solid) and 50 MPa (dashed). Light gray lines = predicted variations for the system apatite-fluid from Piccoli and Candela (1994) at 1 GPa (dashed) and 50 MPa (dotted). Black dotted line shows the  $T$ -only regression. Gray fields show the experimental range of Li and Hermann (2017; 2.5 GPa). Dashed light gray outlines show the experimental range of Li and Hermann (2015; 2.5–4.5 GPa).

**TABLE 4.** Summary of multiple regression results for literature data set of OH-halogen  $K_D$  values ( $T$  in K,  $P$  in bar)

	OH-F		OH-Cl	
	±		±	
Equation 1: $\log K_D = a + b/T + c(P - 1)/T$				
<i>a</i>	1.33	0.2907	1.333	0.234
<i>b</i>	-3864	361	-3344	288
<i>c</i>	0.01532	0.007218	0.01038	0.002746
Equation 2: $\log K_D = a + b/T$				
<i>a</i>	1.259	0.2942	1.0729	0.2353
<i>b</i>	-3853.6	368	-2938	282

(Piccoli and Candela 1994) than for apatite–melt (literature data compilation, Fig. 8). The cause of this mismatch for  $K_D^{\text{OH-F}}$  is unclear, particularly given that there is relatively good agreement for  $K_D^{\text{OH-Cl}}$  at low temperatures (where one or more fluid phases are most likely to be present). Calculating  $K_D$  values using OH and halogen mole fractions instead of  $\text{H}_2\text{O}_i$  results in higher values in Figure 8. The experiments do not contain any other phases that could incorporate significant F. Our calculations (together with those of the other studies in the literature) were done using melt F concentrations instead of activities, and fluoride activity varies with both melt composition (e.g., Scaillet and Macdonald 2004) and temperature (e.g., Webster 1990). Piccoli and Candela (1994) attempted to apply their method to the Bishop Tuff and found similar problems, with good agreement between predicted (from apatite) and measured (from melt inclusions) Cl concentrations, but a much wider discrepancy for F, which they interpreted as a problem with the assumption that F is present only as HF in the fluid. We therefore suggest that improved fluoride activity and speciation models for silicate melts and fluids may help to resolve this problem.

### IMPLICATIONS

Recent experimental studies of apatite–melt partitioning have greatly enhanced the potential of apatite as a tool for interpreting magmatic volatile contents, in both terrestrial and planetary settings (Piccoli and Candela 1994; Boyce and Hervig 2008; McCubbin et al. 2015). The results presented here extend this work to the important magmatic volatile C, which records key information regarding deep magma storage and early degassing processes. Our new partitioning experiments on haplobasaltic andesite and trachyte melts provide the first constraints on partitioning mechanisms and exchange coefficients for C in high-temperature igneous apatite. Stoichiometry calculations and preliminary FTIR-ATR analysis indicates that carbonate is accommodated primarily in the c-axis channel in our experiments. OH calculated by difference agrees relatively well with measured OH for the halogen-bearing experiments but is systematically low for the halogen-free experiments. This suggests the presence of a significant oxyapatite component at high temperatures, and emphasizes that calculations of OH by difference should be treated with care. Analysis of C in apatite represents a potential new route to better understanding the original  $\text{CO}_2$  contents of melts, particularly in arc systems, where melt inclusion  $\text{CO}_2$  concentrations likely represent a significant underestimate of  $\text{CO}_2$  in the un-degassed melt. The ease of SIMS analysis, as demonstrated here, should facilitate this goal, particularly for small natural crystals and inclusions within phenocrysts. We encourage future work comparing  $\text{CO}_2$  in arc melt inclusions with  $\text{CO}_2$  inferred from coexisting apatite inclusions, and suggest that this may help to improve our understanding of volatile fluxes at subduction zones.

Regression of our new partitioning data, alongside previously published experimental data in the system apatite–silicate melt, shows that while measurements of Cl–OH exchange are in good agreement with existing estimates for the system apatite–fluid (Piccoli and Candela 1994), there is a large discrepancy for F–OH exchange, which may be due to a relatively poor understanding of the fluoride activity and speciation in silicate melts and fluids. This highlights the need for further experimental work focused on clarifying the mobility and compatibility of halogens between solids, melt, and fluids close to the magmatic-hydrothermal transi-

tion. Nonetheless, the current study marks a significant advance in the understanding of volatile partitioning in high-temperature igneous apatites and opens up the potential for quantitative analysis and modeling of magmatic volatile systematics in both terrestrial and extraterrestrial environments. Apatite can accommodate the full range of volatile elements and, in our view, future work should focus on the quantitative modeling of variations in apatite composition during common igneous processes such as cooling, ascent, and degassing of fluid(s), with the aim of fully developing apatite as a tool for investigating magmatic storage and degassing processes.

### ACKNOWLEDGMENTS

This project was funded by the Natural Environment Research Council under grants NE/K003852/1 and NE/K004786/1, as well as multiple visits to the NERC ion microprobe facility at University of Edinburgh. M.C.S.H. was supported by a Royal Society University Research Fellowship. We are grateful to Stuart Kearns for analytical support for the electron microprobe, and to Francis McCubbin and Victoria Smith for useful discussions. We acknowledge Bernie Wood and Andrew Matzen for access to the high-temperature gas-mixing furnace at University of Oxford, and Niccy Potts for access to her unpublished experimental distribution coefficients. We thank Francis McCubbin and Adam Simon for journal reviews that helped to clarify the manuscript, and Dan Harlov for his editorial contributions. Finally, M.C.S.H. is grateful to Tom Sisson and Tim Grove for, in a previous decade, encouraging a study of volatiles in apatite.

### REFERENCES CITED

- Aster, E.M., Wallace, P.J., Moore, L.R., Watkins, J., Gazel, E., and Bodnar, R.J. (2016) Reconstructing  $\text{CO}_2$  concentrations in basaltic melt inclusions using Raman analysis of vapor bubbles. *Journal of Volcanology and Geothermal Research*, 323, 148–162.
- Binder, G., and Troll, G. (1989) Coupled anion substitution in natural carbon-bearing apatites. *Contributions to Mineralogy and Petrology*, 101, 394–401.
- Blundy, J., Cashman, K.V., Rust, A., and Witham, F. (2010) A case for  $\text{CO}_2$ -rich arc magmas. *Earth and Planetary Science Letters*, 290, 289–301.
- Bonel, G. (1972) Contribution à l'étude de la carbonatation des apatites. 1. Synthèse et étude des propriétés physico-chimiques des apatites carbonatées du Type A. *Annales de Chimie*, 7, 65–88.
- Boyce, J.W., and Hervig, R.L. (2008) Magmatic degassing histories from apatite volatile stratigraphy. *Geology*, 36, 63–66.
- Boyd, F.R., and England, J.L. (1960) Apparatus for phase-equilibrium measurements at pressures up to 50 kilobars and temperatures up to 1750 °C. *Journal of Geophysical Research*, 65, 741–748.
- Brooker, R.A., and Kjarsgaard, B.A. (2011) Silicate-carbonate liquid immiscibility and phase relations in the system  $\text{SiO}_2$ – $\text{Na}_2\text{O}$ – $\text{Al}_2\text{O}_3$ – $\text{CaO}$ – $\text{CO}_2$  at 0.1–2.5 GPa with applications to carbonatite genesis. *Journal of Petrology*, 52, 1281–1305.
- Brooker, R., Holloway, J.R., and Hervig, R. (1998) Reduction in piston-cylinder experiments: The detection of carbon infiltration into platinum capsules. *American Mineralogist*, 83, 985–994.
- Brooker, R.A., Kohn, S.C., Holloway, J.R., McMillan, P.F., and Carroll, M.R. (1999) Solubility, speciation and dissolution mechanisms for  $\text{CO}_2$  in melts on the  $\text{NaAlO}_2$ – $\text{SiO}_2$  join. *Geochimica et Cosmochimica Acta*, 63, 3549–3565.
- Bureau, H., Metrich, N., Semet, M.P., and Staudacher, T. (1999) Fluid–magma decoupling in a hot-spot volcano. *Geophysical Research Letters*, 26, 3501–3504.
- Collins, S.J., Pyle, D.M., and MacLennan, J. (2009) Melt inclusions track pre-eruption storage and dehydration of magmas at Etna. *Geology*, 37, 571–574.
- De Maeyer, E.A.P., Verbeeck, R.M.H., and Naessens, D.E. (1993) Stoichiometry of  $\text{Na}^+$  and  $\text{CO}_3^{2-}$  containing apatites obtained by hydrolysis of monetite. *Inorganic Chemistry*, 32, 5709–5714.
- Devine, J.D., Gardner, J.E., Brack, H.P., Layne, G.D., and Rutherford, M.J. (1995) Comparison of microanalytical methods for estimating  $\text{H}_2\text{O}$  contents of silicic volcanic glasses. *American Mineralogist*, 80, 319–328.
- Doherty, A.L., Webster, J.D., Goldoff, B.A., and Piccoli, P.M. (2014) Partitioning behavior of chlorine and fluorine in felsic melt–fluid(s)–apatite systems at 50 MPa and 850–950 °C. *Chemical Geology*, 384, 94–111.
- Fabrizio, A., and Carroll, M.R. (2008) Experimental constraints on the differentiation process and pre-eruptive conditions in the magmatic system of Phlegraean Fields (Naples, Italy). *Journal of Volcanology and Geothermal Research*, 171, 88–102.
- Fleet, M.E. (2017) Infrared spectra of carbonate apatites: Evidence for a connection between bone mineral and body fluids. *American Mineralogist*, 102, 149–157.
- Fleet, M.E., Liu, X., and King, P.L. (2004) Accommodation of the carbonate ion in apatite: An FTIR and X-ray structure study of crystals synthesized at 2–4 GPa. *American Mineralogist*, 89, 1422–1432.
- Gaetani, G.A., O'Leary, J.A., Shimizu, N., Bucholz, C.E., and Newville, M. (2012) Rapid reequilibration of  $\text{H}_2\text{O}$  and oxygen fugacity in olivine-hosted melt inclusions. *Geology*, 40, 915–918.
- Goldoff, B., Webster, J.D., and Harlov, D.E. (2012) Characterization of fluor-chlorapatites by electron probe microanalysis with a focus on time-dependent intensity variation

- of halogens. *American Mineralogist*, 97, 1103–1115.
- Hall, L.J., Brodie, J., Wood, B.J., and Carroll, M.R. (2004) Iron and water losses from hydrous basalts contained in  $\text{Au}_{80}\text{Pd}_{20}$  capsules at high pressure and temperature. *Mineralogical Magazine*, 68, 75–81.
- Hartley, M.E., MacLennan, J., Edmonds, M., and Thordarson, T. (2014) Reconstructing the deep  $\text{CO}_2$  degassing behaviour of large basaltic fissure eruptions. *Earth and Planetary Science Letters*, 393, 120–131.
- Hauri, E., Wang, J., Dixon, J.E., King, P.L., Mandeville, C., and Newman, S. (2002) SIMS analysis of volatile in silicate glasses 1. Calibration, matrix effects and comparisons with FTIR. *Chemical Geology*, 183, 99–114.
- Hudgins, T.R., Mukasa, S.B., Simon, A.C., Moore, G., and Barfajio, E. (2015) Melt inclusion evidence for  $\text{CO}_2$ -rich melts beneath the western branch of the East African Rift: implications for long-term storage of volatiles in the deep lithospheric mantle. *Contributions to Mineralogy and Petrology*, 169, 46.
- Hui, H., Zhang, Y., Xu, Z., and Behrens, H. (2008) Pressure dependence of the speciation of dissolved water in rhyolitic melts. *Geochimica et Cosmochimica Acta*, 72, 3229–3240.
- Humphreys, M., Kearns, S., and Blundy, J. (2006) SIMS investigation of electron-beam damage to hydrous, rhyolitic glasses: Implications for melt inclusion analysis. *American Mineralogist*, 91, 667–679.
- Hunt, J.B., and Hill, P.G. (1993) Tephra geochemistry: a discussion of some persistent analytical problems. *The Holocene*, 3, 271–278.
- Ketcham, R.A. (2015) Technical Note: Calculation of stoichiometry from EMP data for apatite and other phases with mixing on monovalent anion sites. *American Mineralogist*, 100, 1620–1623.
- Konecke, B.A., Fiege, A., Simon, A.C., Parat, F., and Stechern, A. (2017) Co-variability of  $\text{S}^{6-}$ ,  $\text{S}^{4-}$ , and  $\text{S}^{2-}$  in apatite as a function of oxidation state: Implications for a new oxybarometer. *American Mineralogist*, 102, 548–557.
- Kubota, T., Nakamura, A., Toyoura, K., and Matsunaga, K. (2014) The effect of chemical potential on the thermodynamic stability of carbonate ions in hydroxyapatite. *Acta Biomaterialia*, 10, 3716–3722.
- LeGeros, R.Z., Trautz, O.R., Klein, E., and LeGeros, J.P. (1969) Two types of carbonate substitution in the apatite structure. *Specialia, Experientia*, 25, 5, <https://doi.org/10.1007/BF01903856>.
- Li, H., and Hermann, J. (2015) Apatite as an indicator of fluid salinity: An experimental study of chlorine and fluorine partitioning in subducted sediments. *Geochimica et Cosmochimica Acta*, 166, 267–297.
- (2017) Chlorine and fluorine partitioning between apatite and sediment melt at 2.5 GPa, 800 °C: A new experimentally derived thermodynamic model. *American Mineralogist*, 102, 580–594.
- MacLennan, J. (2017) Bubble formation and decrepitation control the  $\text{CO}_2$  content of olivine-hosted melt inclusions. *Geochemistry, Geophysics, Geosystems*, 18, 597–616.
- Mangan, M., and Sisson, T. (2000) Delayed, disequilibrium degassing in rhyolite magma: decompression experiments and implications for explosive volcanism. *Earth and Planetary Science Letters*, 183, 441–455.
- Marks, M.A.W., Wenzel, T., Whitehouse, M.J., Loose, M., Zack, T., Barth, M., Worgard, L., Krasz, V., Eby, G.N., Stosnach, H., and others. (2012) The volatile inventory (F, Cl, Br, S, C) of magmatic apatite: An integrated analytical approach. *Chemical Geology*, 291, 241–255.
- Mason, H.E., McCubbin, F.M., Smirnov, A., and Phillips, B.L. (2009) Solid-state NMR and IR spectroscopic investigation of the role of structural water and F in carbonate-rich fluorapatite. *American Mineralogist*, 94, 507–516.
- Mathez, E.A., and Webster, J.D. (2005) Partitioning behavior of chlorine and fluorine in the system apatite–silicate melt–fluid. *Geochimica et Cosmochimica Acta*, 69, 1275–1286.
- Matsunaga, K., and Kuwabara, A. (2007) First principles study of vacancy formation in hydroxyapatite. *Physical Review B*, 75, 014102.
- McCubbin, F.M., Vander Kaaden, K., Tartese, R., Boyce, J.W., Mikhail, S., Whitson, E.S., Bell, A.S., Anand, M., Franchi, I.A., Wang, J., and others. (2015) Experimental investigation of F, Cl, and OH partitioning between apatite and Fe-rich basaltic melt at 1.0–1.2 GPa and 950–1000 °C. *American Mineralogist*, 100, 1790–1802.
- McDade, P., Wood, B.J., van Westrenen, W., Brooker, R., Gudmundsson, G., Soular, H., Najorka, J., and Blundy, J. (2002) Pressure corrections for a selection of piston-cylinder cell assemblies. *Mineralogical Magazine*, 66, 1021–1028.
- Mills, R.D., and Glazner, A.F. (2013) Experimental study on the effects of temperature cycling on coarsening of plagioclase and olivine in an alkali basalt. *Contributions to Mineralogy and Petrology*, 166, 97–111.
- Moore, L.R., Gazel, E., Tuohy, R., Lloyd, A.S., Esposito, R., Steele-MacInnis, M., Hauri, E.H., Wallace, P.J., Plank, T., and Bodnar, R.J. (2015) Bubbles matter: An assessment of the contribution of vapor bubbles to melt inclusion volatile budgets. *American Mineralogist*, 100, 806–823.
- Morgan, G.B., and London, D. (1996) Optimizing the electron microprobe analysis of hydrous alkali aluminosilicate glasses. *American Mineralogist*, 81, 1176–1185.
- Morizet, Y., Brooker, R.A., and Kohn, S.C. (2002)  $\text{CO}_2$  in haplo-phonolite melt: solubility, speciation and carbonate complexation. *Geochimica et Cosmochimica Acta*, 66, 1809–1820.
- Pan, Y., and Fleet, M.E. (2002) Compositions of the apatite-group minerals: substitution mechanisms and controlling factors. *Reviews in Mineralogy and Geochemistry*, 48, 13–49.
- Peng, G., Luhr, J.F., and McGee, J.J. (1997) Factors controlling sulfur concentrations in volcanic apatite. *American Mineralogist*, 82, 1210–1224.
- Peroos, S., Du, Z., and de Leeuw, N.H. (2006) A computer modelling study of the uptake, structure and distribution of carbonate defects in hydroxy-apatite. *Biomaterials*, 27, 2150–2161.
- Piccoli, P., and Candela, P. (1994) Apatite in felsic rocks: A model for the estimation of initial halogen concentrations in the Bishop Tuff (Long Valley) and Tuolumne Intrusive Suite (Sierra Nevada Batholith) magmas. *American Journal of Science*, 294, 92–135.
- Potts, N.J., van Westrenen, W., Tart, R., Franchi, I.A., and Anand, M. (2015) Apatite–melt volatile partitioning under lunar conditions. *Proceedings of the 46th Lunar and Planetary Science Conference*, 1372.
- Prowatke, S., and Klemme, S. (2006) Trace element partitioning between apatite and silicate melts. *Geochimica et Cosmochimica Acta*, 70, 4513–4527.
- Robie, R.A., Hemingway, B.S., and Fisher, J.F. (1978) Thermodynamic properties of minerals and related substances at 298.15 K and 1 bar ( $10^5$  Pascals) pressure and at higher temperature. *US Geological Survey Bulletin*, 1452.
- Roeber, P.L., and Emslie, R.F. (1970) Olivine–liquid equilibrium. *Contributions to Mineralogy and Petrology*, 29, 275–289.
- Scaillat, B., and MacDonald, R. (2004) Fluorite stability in silicic magmas. *Contributions to Mineralogy and Petrology*, 147, 319–329.
- Schettler, G., Gottschalk, M., and Harlov, D.E. (2011) A new semi-micro wet chemical method for apatite analysis and its application to the crystal chemistry of fluorapatite–chlorapatite solid solutions. *American Mineralogist*, 96, 138–152.
- Shishkina, T.A., Botcharnikov, R.E., Holtz, R., Almeev, R.R., and Portnyagin, M.V. (2010) Solubility of  $\text{H}_2\text{O}$ - and  $\text{CO}_2$ -bearing fluids in tholeiitic basalts at pressures up to 500 MPa. *Chemical Geology*, 277, 115–125.
- Sowerby, J.R., and Keppler, H. (1999) Water speciation in rhyolitic melt determined by in-situ infrared spectroscopy. *American Mineralogist*, 84, 1843–1849.
- Spilliaert, N., Allard, P., Metrich, N., and Sobolev, A.V. (2006) Melt inclusion record of the conditions of ascent, degassing, and extrusion of volatile-rich alkali basalt during the powerful 2002 flank eruption of Mount Etna (Italy). *Journal of Geophysical Research*, 111, B04203.
- Stock, M.J., Humphreys, M.C.S., Smith, V.C., Johnson, R.D., Pyle, D.M., and EIMF (2015) New constraints on electron-beam induced halogen migration in apatite. *American Mineralogist*, 100, 281–293.
- Stull, D.R., and Prophet, H. (1971) JANAF thermochemical tables (no. NSRDS-NBS-37). National Standard Reference Data System.
- Swanson, S.E. (1977) Relation of nucleation and crystal-growth rate to the development of granitic textures. *American Mineralogist*, 62, 966–978.
- Trombe, J.C., and Montel, G. (1978) Some features of the incorporation of oxygen in different oxidation states in the apatite lattice—I. On the existence of calcium and strontium oxyapatites. *Journal of Inorganic and Nuclear Chemistry*, 40, 15–21.
- Tuohy, R., Wallace, P.J., Loewen, M.W., Swanson, D.A., and Kent, A.J.R. (2016) Magma transport and olivine crystallization depths in Kilauea's east rift zone inferred from experimentally rehomogenized melt inclusions. *Geochimica et Cosmochimica Acta*, 185, 232–250.
- Wallace, P.J. (2005) Volatiles in subduction zone magmas: concentrations and fluxes based on melt inclusion and volcanic gas data. *Journal of Volcanology and Geothermal Research*, 140, 217–240.
- Wallace, P.J., Kamenetsky, V.S., and Cervantes, P. (2015) Melt inclusion  $\text{CO}_2$  contents, pressures of olivine crystallization, and the problem of shrinkage bubbles. *American Mineralogist*, 100, 787–794.
- Webster, J.D. (1990) Partitioning of F between  $\text{H}_2\text{O}$  and  $\text{CO}_2$  fluids and topaz rhyolite melt. Implications for mineralizing magmatic-hydrothermal fluids in F-rich granitic systems. *Contributions to Mineralogy and Petrology*, 104, 424–438.
- Webster, J.D., Tappen, C.M., and Mandeville, C.W. (2009) Partitioning behavior of chlorine and fluorine in the system apatite–melt–fluid. II: Felsic silicate systems at 200 MPa. *Geochimica et Cosmochimica Acta*, 73, 559–581.
- Webster, J.D., Goldoff, B.A., Flesch, R.N., Nadeau, P.A., and Silbert, Z.W. (2017) Hydroxyl, Cl, and F partitioning between high-silica rhyolitic melts–apatite–fluid(s) at 50–200 MPa and 700–1000 °C. *American Mineralogist*, 102, 61–74.
- Yoder, C.H., Pasteris, J.D., Worcester, K.N., and Schermerhorn, D.V. (2012) Structural water in carbonated hydroxylapatite and fluorapatite: confirmation by solid state  $^1\text{H}$  NMR. *Calcified Tissue International*, 90, 60–67.
- Young, R.A., Bartlett, M.E., Spooner, S., Mackie, P.E., and Bonel, G. (1981) Reversible high temperature exchange of carbonate and hydroxyl ions in tooth enamel and synthetic hydroxyapatite. *Journal of Biological Physics*, 9, 1–26.
- Zhu, C., and Sverjensky, D.A. (1991) Partitioning of F–Cl–OH between minerals and hydrothermal fluids. *Geochimica et Cosmochimica Acta*, 55, 1837–1858.

MANUSCRIPT RECEIVED MAY 9, 2017

MANUSCRIPT ACCEPTED OCTOBER 7, 2017

MANUSCRIPT HANDLED BY DANIEL HARLOW

## Endnote:

<sup>1</sup>Deposit item AM-18-26187, Supplemental Material. Deposit items are free to all readers and found on the MSA web site, via the specific issue's Table of Contents (go to [http://www.minsocam.org/MSA/AmMin/TOC/2018/Feb2018\\_data/Feb2018\\_data.html](http://www.minsocam.org/MSA/AmMin/TOC/2018/Feb2018_data/Feb2018_data.html)).